Mine subsidence monitoring and prediction integrating SBAS-InSAR technology and BO-Prophet model

Kangjie Yu

College of Geographic Sciences, Shanxi Normal University, Taiyuan City, Shanxi Province, China

ABSTRACT

Coal mining causes significant environmental disruptions due to excessive resource extraction. Real-time monitoring and prediction of mining-induced surface deformation are critical for ensuring mining safety. Conventional monitoring methods struggle to achieve large-scale real-time observation and have limitations in terrain adaptability and weather resistance. Conventional prediction methods are constrained as follows: numerical simulation is limited by the complexity of physical parameters; mathematical statistics requires substantial data and struggles to comprehensively reflect geotechnical properties; hybrid algorithms involve complex modeling and rely on individual models. This study develops an integrated framework combining Small Baseline Subset Interferometric Synthetic Aperture Radar (SBAS-InSAR) and Bayesian optimization-Prophet (BO-Prophet) models for mining subsidence monitoring and forecasting. Using the Yinying Coal Mine as the study area, multi-source radar datasets are processed through SBAS-InSAR. This technique identifies four major subsidence areas and generates time-series deformation data. Cross-validation confirms the reliability of SBAS-InSAR monitoring results: the Pearson correlation coefficient between ascending-orbit (Sentinel-1A) and descending-orbit (Radarsat-2) results of 3,000 high-coherence points in the subsidence area reaches 0.946; compared with four Global Navigation Satellite System (GNSS) stations, the maximum absolute errors are 4.684, 3.328, 3.194, and 2.462 mm respectively, with consistent deformation trends, and both methods confirm its reliability. Comparative analysis reveals superior prediction accuracy of the BO-Prophet model over Bayesian optimization-long short-term memory (BO-LSTM) at six characteristic points. The BO-Prophet model achieves a mean absolute error (MAE) of 2.02 mm, representing a 25.2% reduction from BO-LSTM (2.70 mm). Its root mean square error (RMSE) measures 2.36 mm, demonstrating a 35.6% reduction compared to BO-LSTM (3.67 mm). Subsidence predictions for area B using BO-Prophet show high spatial-temporal consistency with SBAS-InSAR monitoring results. Correlation analysis demonstrates a correlation coefficient (R^2) exceeding 0.96 between predicted and observed values. The integration of SBAS-InSAR and BO-Prophet shows strong potential for mining subsidence monitoring and forecasting. This combined approach enhances early warning capabilities and supports disaster mitigation strategies in mining areas.

Subjects Artificial Intelligence, Computer Vision, Data Mining and Machine Learning, Spatial and Geographic Information Systems

Keywords Subsidence monitoring, SBAS-InSAR, Subsidence prediction, BO-Prophet, Coal mining

Submitted 27 March 2025
Accepted 3 October 2025
Published 28 October 2025

Corresponding author
Kangjie Yu,
m18536497390@163.com

Academic editor
Feng Gu

Additional Information and Declarations can be found on page 21

DOI **10.7717/peerj-cs.3327**

How to cite this article Yu K. 2025. Mine subsidence monitoring and prediction integrating SBAS-InSAR technology and BO-Prophet model. **PeerJ Comput. Sci. 11:e3327 DOI 10.7717/peerj-cs.3327**

INTRODUCTION

Coal, as a crucial mineral resource in China, holds absolute dominance in the national energy structure and plays an irreplaceable role in social development and economic construction. Shanxi Province contributes approximately one-quarter of China's coal production, serving as a vital national energy base (*Bai et al., 2020*). However, excessive coal mining has triggered ground collapse, air pollution, farmland destruction, and geological hazards like landslides and mudslides, severely threatening local residents' safety and quality of life (*Chu & Muradian, 2016*; *Dontala, Reddy & Vadde, 2015*; *Habib & Khan, 2021*). Real-time monitoring and prediction of surface deformation are essential for preventing geological disasters and ensuring mining safety.

Traditional monitoring methods like precise leveling and GPS measurements face limitations in terrain adaptability, weather resistance, and spatial coverage (*Santos, Cabral & Pontes Filho, 2012*; *Sevil, Benito-Calvo & Gutiérrez, 2021*). These point/line-based approaches struggle to achieve large-scale monitoring and fail to reflect comprehensive deformation patterns across mining areas. High costs, low efficiency, and limited coverage further restrict their application in long-term, large-area subsidence monitoring.

Interferometric synthetic aperture radar (InSAR) overcomes these limitations by enabling cost-effective, weather-independent large-area monitoring with comprehensive surface deformation insights (*Aobpaet et al., 2013*; *Wu, Wei & D'Hondt, 2022*). D-InSAR generates interferograms to separate terrain features from deformation signals, supporting continuous long-term monitoring (*Fan et al., 2011*; *Zhu et al., 2024*). However, its accuracy suffers from image decorrelation and atmospheric delays (*Cai et al., 2023*). PS-InSAR achieves high-precision deformation monitoring by identifying persistent scatterers (buildings, bare rocks) with stable phase characteristics, which effectively mitigates atmospheric phase errors. However, in mining areas with high vegetation coverage, the scarcity of such persistent scatterers leads to sparse monitoring points, failing to capture the overall subsidence patterns (*Liu et al., 2022*). DS-InSAR improves monitoring point density by identifying distributed scatterers (vegetated areas with weak scattering targets), particularly outperforming PS-InSAR in vegetated zones. However, it still struggles with spatial decorrelation in steep terrains or areas with severe atmospheric delays, compromising accuracy in mountainous mining regions (*Li et al., 2021*). In mining area subsidence monitoring, SBAS-InSAR demonstrates strong adaptability to complex environments. For mountainous mining areas with rugged terrain and high vegetation coverage, SBAS-InSAR effectively reduces temporal and spatial decorrelation by controlling small spatiotemporal baselines. It generates continuous high-temporal-resolution deformation time series to capture dynamic subsidence from mining activities, and adapts flexibly to moderate data volumes, balancing monitoring accuracy and regional coverage (*Du et al., 2021*; *Khan et al., 2025*; *Li, Xu & Li, 2022*). Unlike DS-InSAR, which may fail in large deformation zones due to insufficient coherence, SBAS-InSAR maintains reliable results across diverse mining scenarios. This makes it more suitable for subsidence monitoring in such complex mining environments compared to D-InSAR, PS-InSAR, and DS-InSAR. This SBAS-InSAR approach has gained widespread recognition in mine monitoring.

Surface subsidence prediction methods include numerical simulation, mathematical statistics, Hybrid algorithms, and machine learning models (*Cai et al., 2023*; *Wang et al., 2025*). Numerical simulation methods analyze stress distribution in mining areas through numerical modeling, yet their effectiveness is limited by the complexity of physical parameters (*He, Wu & Ma, 2023*; *Li, Zha & Guo, 2019*). Mathematical statistical methods offer intuitive data-driven solutions; however, they demand substantial observational data and struggle to comprehensively characterize geotechnical medium properties, thereby compromising prediction reliability (*Hejmanowski & Malinowska, 2009*). Hybrid algorithms enhance accuracy and stability by integrating multiple model outputs, though they entail complex modeling structures and remain dependent on individual model performance (*Shen, Santosh & Arabameri, 2023*).

In recent years, machine learning models have demonstrated remarkable potential in surface deformation prediction (*Deng et al., 2025*; *Wang et al., 2024*; *Yang et al., 2025*), particularly in addressing multi-factor induced surface deformations. The large-scale, high-precision surface deformation data acquired through InSAR technology provides abundant training samples for machine learning models (*Guo et al., 2023*; *Shi et al., 2020*, *2023*). Assessing the applicability of machine learning models for mining subsidence prediction requires comprehensive consideration of environmental characteristics and data attributes. Grey models (GM) are based on grey system theory. GM suits scenarios with limited samples or missing information. For example, *Shi et al. (2020)* integrated D-InSAR technology with the GM(1,1) model to achieve unified subsidence monitoring and prediction. However, GM exhibits poor prediction stability and struggles to capture nonlinear dynamic deformations. Support vector regression (SVR) can map high-dimensional nonlinear relationships and possesses good robustness. *Zhang et al. (2021)* successfully predicted subsidence in Shaanxi mining areas using SBAS-InSAR and SVR. Nevertheless, SVR demands substantial computational resources. It also shows insufficient adaptability to sudden subsidence events in long time series. Long short-term memory (LSTM) networks perform well in learning mining subsidence patterns. *Ma, Sui & Lian (2023)* confirmed through comparative experiments that LSTM outperforms SVR. However, *Dongwei et al. (2024)* noted LSTM's susceptibility to spatial heterogeneity and feature deficiencies, these limitations can cause significant accuracy reductions. In contrast, the Prophet model employs Bayesian curve fitting *via* a generalized additive model. Prophet offers notable flexibility and robustness. Its built-in trend decomposition module accurately distinguishes subsidence caused by natural and anthropogenic factors (*Bi et al., 2024*).

Hyperparameter selection significantly impacts prediction model performance. Research by *Chen et al. (2025)* demonstrated that hyperparameter optimization effectively enhances model prediction capability. Subjective hyperparameter selection proves inefficient and often suboptimal. Therefore, this study introduces Bayesian optimization

(BO) for hyperparameter tuning. This method efficiently explores the parameter space. BO achieves relatively optimal parameter combinations with fewer evaluations and lower time costs. To highlight the advantages of the proposed Bayesian optimization-Prophet (BO-Prophet) model for mining subsidence prediction, we conducted a comparative analysis. We compared its performance against Bayesian optimization-long short-term memory (BO-LSTM), an LSTM model also optimized with Bayesian optimization.

This study focuses on Yangquan's Yinying mining area, utilizing 34 ascending Sentinel-1A radar images and 17 descending radar RADARSAT-2 images for SBAS-InSAR processing. The analysis of multi-source data from June 2023 to August 2024 confirms result consistency and reliability. To optimize prediction accuracy, Bayesian optimization adjusts hyperparameters in Prophet and LSTM models. The enhanced models predict subsidence values at selected characteristic points, comparing performance outcomes to provide scientific support for early warning systems.

STUDY AREA

Yinying Coal Mine is located in Yinying Town, northern suburbs of Yangquan City. Its geographic coordinates range from 113°27′17.46″E to 113°33′27.684″E longitude and 37°56′22.754″N to 38°0′36.407″N latitude. The area features a temperate continental monsoon climate with annual average temperatures between 8–12 °C and precipitation ranging 450–550 mm.

The terrain shows northwest-high and southeast-low topography, classified as low mountain hills with elevations spanning 660–1,373 m. Surface coverage primarily consists of forest land and grassland. The mining area covers approximately 19.1 km^2.

As a major coal production base, Yinying Coal Mine maintains an average coal seam thickness of 3.75 m. Coal seams exhibit an average dip angle of approximately three degrees. Annual production capacity reaches 2.4 million tons.

Key geological characteristics include crisscrossing valleys and densely distributed gullies formed by historical river erosion. These geomorphological features contribute to complex mining conditions requiring advanced monitoring systems like SBAS-InSAR for deformation tracking. Figure 1 shows the geographical location and surface conditions of the study area.

DATA SOURCES AND METHODOLOGY

Data sources

This study collected ascending synthetic aperature radar (SAR) data from June 23, 2023 to August 4, 2024 and descending SAR data spanning June 21, 2023 to August 2, 2024. The descending data is used to verify the reliability of ascending monitoring results. The ascending dataset comprises 34 scenes of Sentinel-1A IW-mode images with 20 m spatial resolution. Its 12-day revisit cycle ensures temporal consistency for deformation monitoring. Descending data contains 17 scenes of RADARSAT-2 XF-mode images achieving 5 m resolution. The 24-day revisit cycle provides complementary observation angles. In addition, Precise orbit files were collected to eliminate orbital errors through ESA's Precise Orbit Determination (POD) service. A total of 30 m digital elevation model

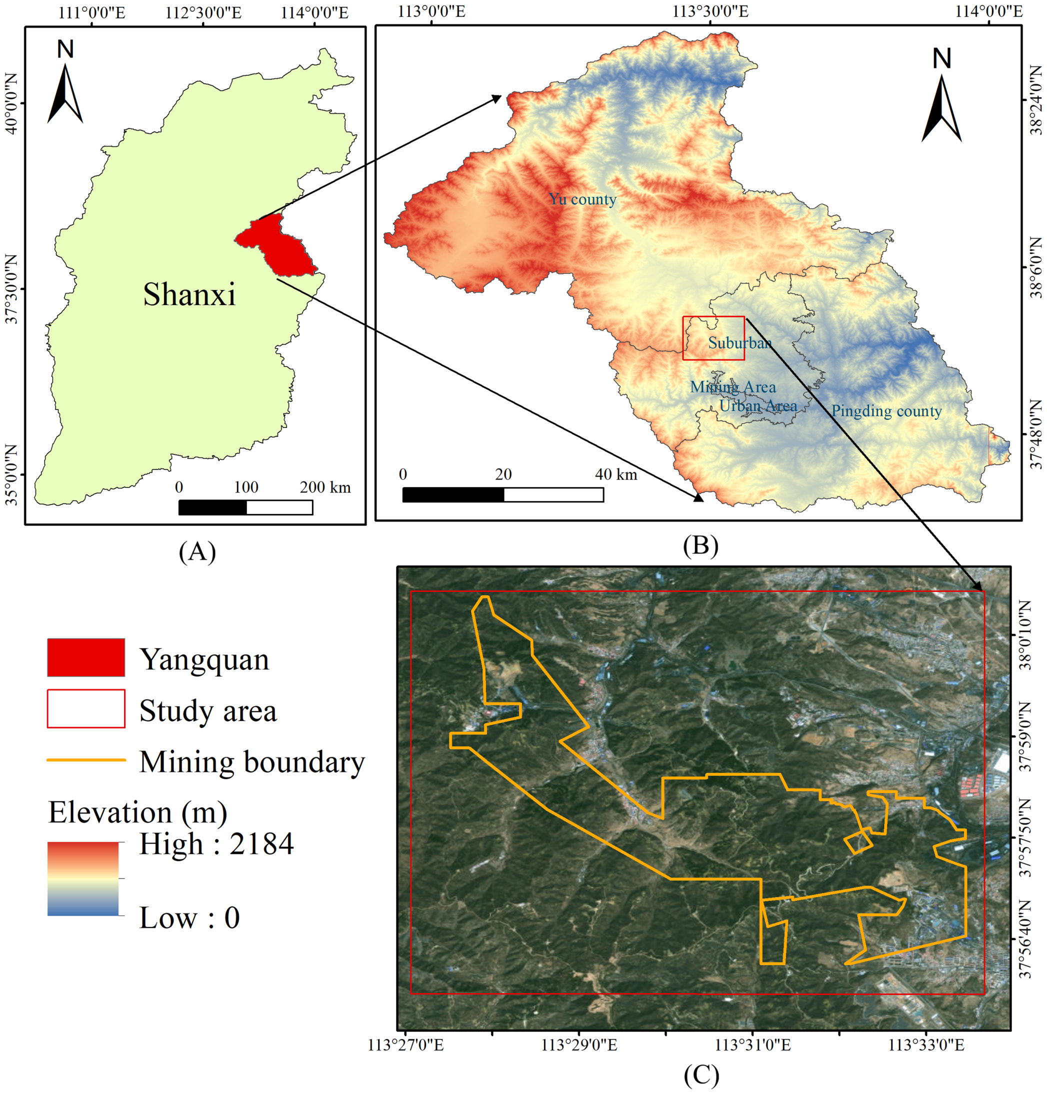

Figure 1 **Location and current status of the study area: (A) Shanxi province; (B) DEM of Yangquan City; (C) study area (red box), Yinying Mining Boundary (orange line).** Satellite image base map from TianDiTu (www.tianditu.gov.cn). Full-size DOI: 10.7717/peerj-cs.3327/fig-1

(DEM) data were obtained to remove topographic phase effects. Table 1 shows the comparison between the two types of data.

SBAS-InSAR

SBAS-InSAR (Small Baseline Subset InSAR) is a time-series InSAR analysis method using multiple master images, *Berardino et al. (2002)* proposed this technology in 2002. Figure 2 shows the SBAS-InSAR workflow. The core principle involves organizing numerous SAR datasets into interferometric subsets. Each subset contains multiple master images. All interferometric pairs in a subset maintain baseline lengths below critical baseline thresholds. The time baselines are also minimized. This approach resolves decorrelation issues in both temporal and spatial dimensions. The method then applies minimum norm

Table 1 Sentinel-1A data parameters and RADARSAT-2 data parameters.

Sensor	Orbital direction	Revisit time	Polarization mode	Imaging mode	Resolution
Sentinel-1A	Ascending	12d	VV + VH	IW	5 m * 20 m
RADARSAT-2	Descending	24d	HH	XF	5 m * 5 m

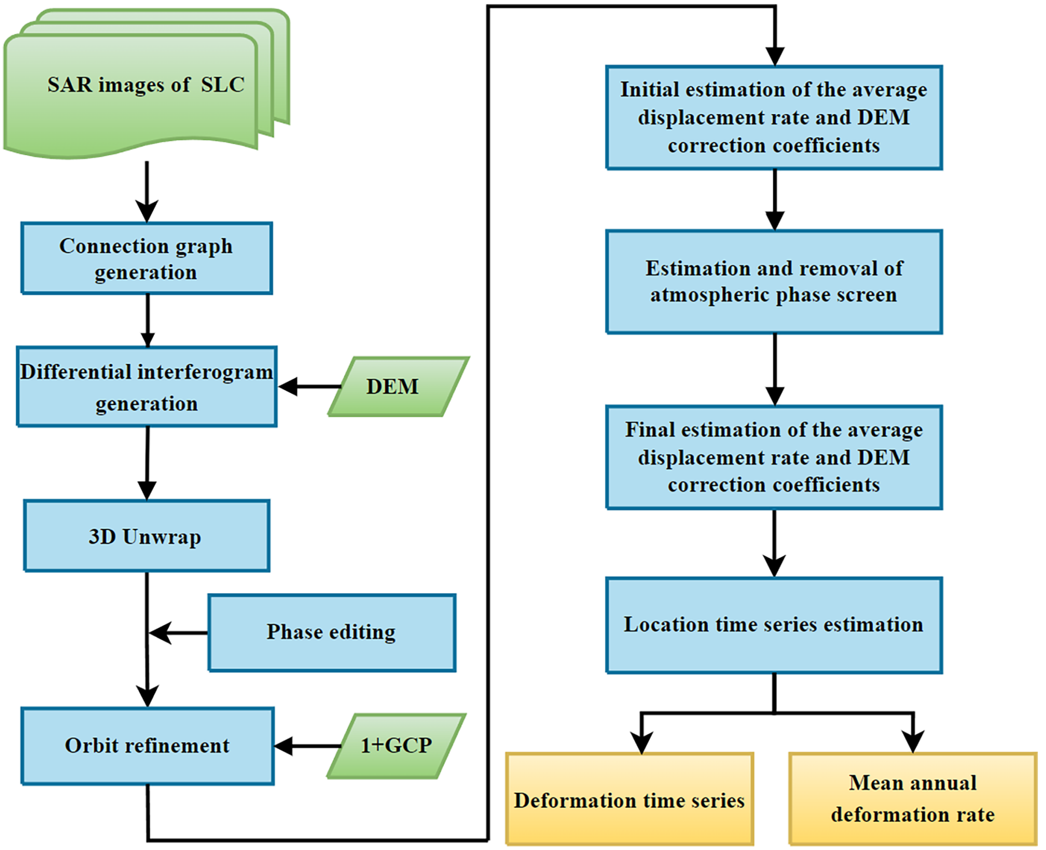

Figure 2 SBAS-InSAR processing flow chart. Full-size DOI: 10.7717/peerj-cs.3327/fig-2

criteria for deformation velocity estimation. Singular value decomposition (SVD) helps obtain time-series deformation of coherent targets. It also generates average deformation rate maps (*Li, Xu & Li, 2022*). SBAS-InSAR achieves reliable monitoring results with relatively small datasets. This technology proves particularly effective for monitoring surface deformation in mining areas.

BO-Prophet prediction model

This study builds BO-Prophet and BO-LSTM models using PyCharm and Python 3.8, primarily employing the Pandas, NumPy, Kats and Ax libraries. The BO-Prophet model combines Bayesian optimization and the Prophet forecasting framework. Facebook released Prophet as an open-source time series prediction tool in 2017 (*Taylor & Letham, 2018*).

The Prophet model uses an additive regression framework. It consists of three core components: trend, seasonality, and holiday effects. This structure enables Prophet to handle diverse forecasting problems with unique characteristics (*Chang, Yang & Zhang, 2025*; *Chérif et al., 2023*). It effectively captures trend changes, seasonal patterns, holidays, and irregular events in time series data. The basic formula of the Prophet model is:

$$y(t) = g(t) + s(t) + h(t) + \varepsilon_t. \tag{1}$$

In the formula, $g(t)$ represents the trend component, modeling non-periodic changes using piecewise linear or logistic regression; $s(t)$ denotes the seasonality component, capturing periodic fluctuations like weekly or yearly cycles; $h(t)$ accounts for holiday effects, addressing impacts from special events; ε_t is the error term, and it is used to represent unpredicted random fluctuations.

The logistic growth model employs a sigmoid function to describe growth patterns. The logistic function (sigmoid) is expressed as:

$$g(t) = \frac{C(t)}{1 + exp\left(-\left(k + a(t)^T\delta\right)\left(t - \left(m + a(t)^T\gamma\right)\right)\right)}. \tag{2}$$

In the formula, $C(t)$ indicates the trend's saturation capacity; k controls the growth rate; m represents the base inflection point parameter of the trend; $a(t)$ serves as the trend's changepoint indicator matrix; δ represents the trend slope adjustment coefficient; γ represents the trend inflection point time adjustment coefficient.

Prophet incorporates Fourier series to model periodic variations. This approach represents seasonality through linear combinations of sine and cosine functions:

$$s(t) = \sum_{n=1}^{N}\left(a_n\, cos\left(\frac{2\pi nt}{P}\right) + b_n\, sin\left(\frac{2\pi nt}{P}\right)\right) = x(t)\beta. \tag{3}$$

In the formula, a_n, b_n represent the Fourier coefficients; P indicates the period length; $x(t)$ serves as the Fourier basis matrix; β denotes parameters following a normal distribution: $\beta \sim N(0, \sigma^2)$; A larger σ amplifies seasonal effects, while a smaller σ reduces them.

Hyperparameters are parameters set before training machine learning models. Their values cannot be learned automatically during training. Researchers select these values based on experience or experimentation (*Bischl et al., 2023*). Manual hyperparameter adjustment is time-consuming and expertise-dependent. BO is an algorithm for finding optimal solutions to functions. It efficiently explores parameter spaces. This method identifies strong parameter combinations with minimal trials and time. It is widely used for hyperparameter tuning in machine learning (*Snoek, Larochelle & Adams, 2012*). BO builds a probabilistic model of the objective function. This model guides the search process. The goal is to find parameter configurations that optimize the objective function. The algorithm handles complex objective functions with multiple peaks or non-convex shapes. It performs effectively in many practical applications (*Shahriari et al., 2015*).

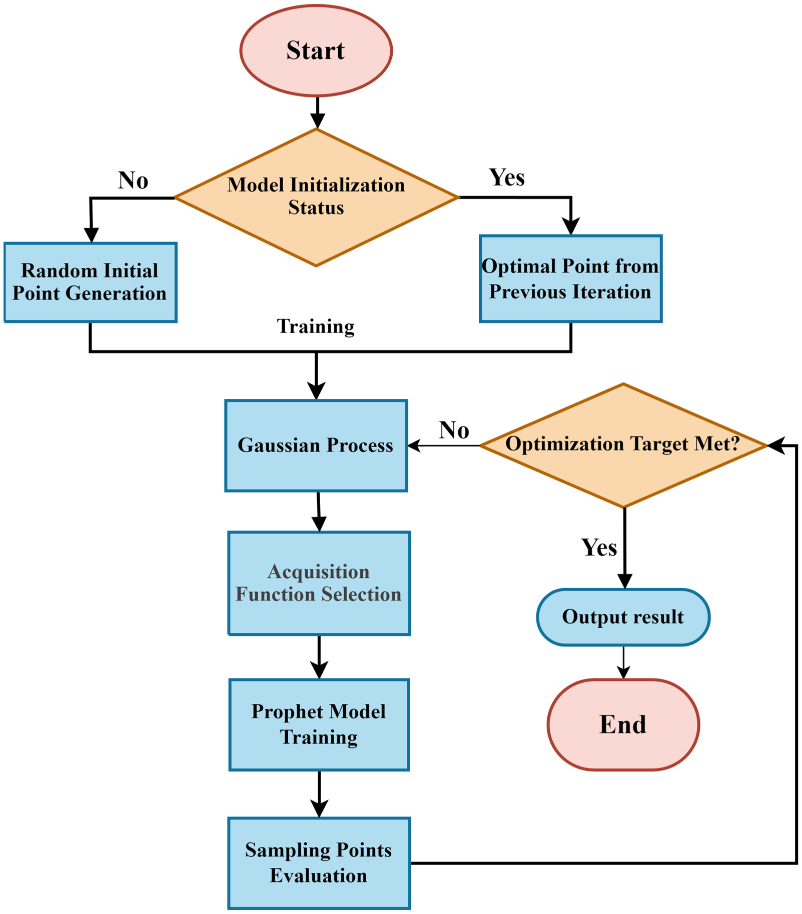

Figure 3 Flowchart of Prophet prediction model algorithm based on Bayesian optimization.
Full-size DOI: 10.7717/peerj-cs.3327/fig-3

The BO-Prophet framework applies BO to tune Prophet hyperparameters, as shown in Fig. 3. The process begins by randomly sampling an initial set of hyperparameters. These hyperparameters initialize the model configuration. The framework then evaluates the model training outcomes using predefined metrics. A Gaussian process model integrates historical hyperparameter evaluations and their performance results. An acquisition function analyzes this probabilistic model. It selects the next hyperparameter set with the highest potential performance improvement. The system iteratively repeats hyperparameter selection, model retraining, and performance evaluation. This loop continues until meeting predefined termination criteria (*e.g.*, maximum iterations or convergence thresholds).

LSTM prediction model

This study compares the LSTM neural network prediction model with the Prophet model. LSTM represents a specialized type of recurrent neural network (RNN) (*Yu et al., 2019*). Compared to conventional RNNs, LSTM demonstrates superior performance in processing time-series data with extended intervals between critical events. The LSTM

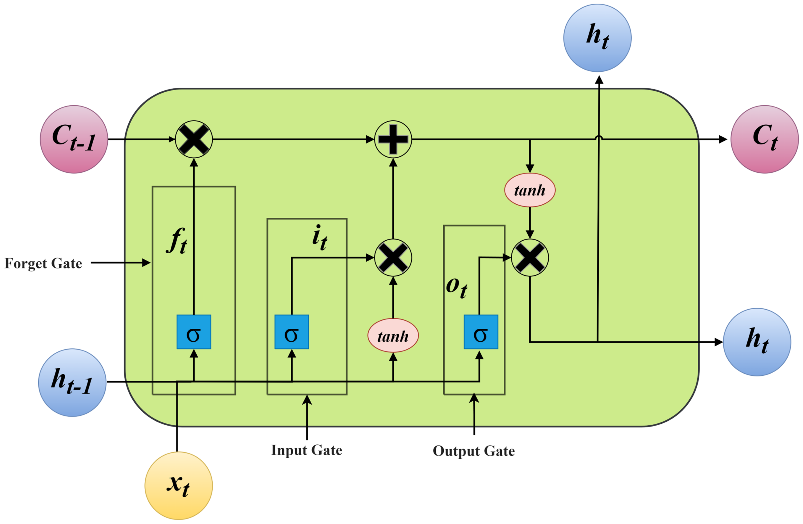

Figure 4 **LSTM unit structure.** Full-size DOI: 10.7717/peerj-cs.3327/fig-4

architecture incorporates memory cells and three gating units. Memory cells store historical information systematically. The input gate regulates the integration of current input data into memory cells. The forget gate manages the elimination of irrelevant information from memory cells (*Smagulova & James, 2019*). The output gate controls the transmission of stored information to subsequent layers. These gating mechanisms collectively preserve crucial temporal patterns in sequences. They effectively address long-term dependency challenges in time-series analysis. Additionally, this structure resolves gradient-related instability problems common in standard RNNs. Figure 4 illustrates the memory unit configuration of the LSTM neural network.

The memory unit structure of LSTM neural networks can be mathematically represented by the following equations:

$$f_t = \sigma\left(W_f[h_{t-1}, x_t] + b_f\right) \tag{4}$$
$$i_t = \sigma(W_i[h_{t-1}, x_t] + b_i) \tag{5}$$
$$\tilde{C}_t = \tanh\,(W_C[h_{t-1}, x_t] + b_C) \tag{6}$$
$$C_t = f_t * C_{t-1} + i_t * \tilde{C}_t \tag{7}$$
$$o_t = \sigma(W_o[h_{t-1}, x_t] + b_o) \tag{8}$$
$$h_t = o_t * \tanh\,(C_t). \tag{9}$$

In the formulas, the notation $[h_{t-1}, x_t]$ represents the concatenated matrix of the previous hidden state h_{t-1} and current input x_t. The variables f_t, i_t, and o_t denote the forget gate, input gate, and output gate values at time step t. The operator σ indicates the Sigmoid activation function. W_f, W_i and W_o are the weight matrices of the forget gate, input gate and output gate, respectively; W_C is the weight matrix for the candidate memory cell $\tilde{C}_t$, acting on the concatenated matrix $[h_{t-1}, x_t]$. b_f, b_i and b_o are the bias terms of the forget gate, input gate and output gate, respectively; b_C is the bias term for the candidate memory cell $\tilde{C}_t$. C_t represents the memory cell state at time step t, which retains

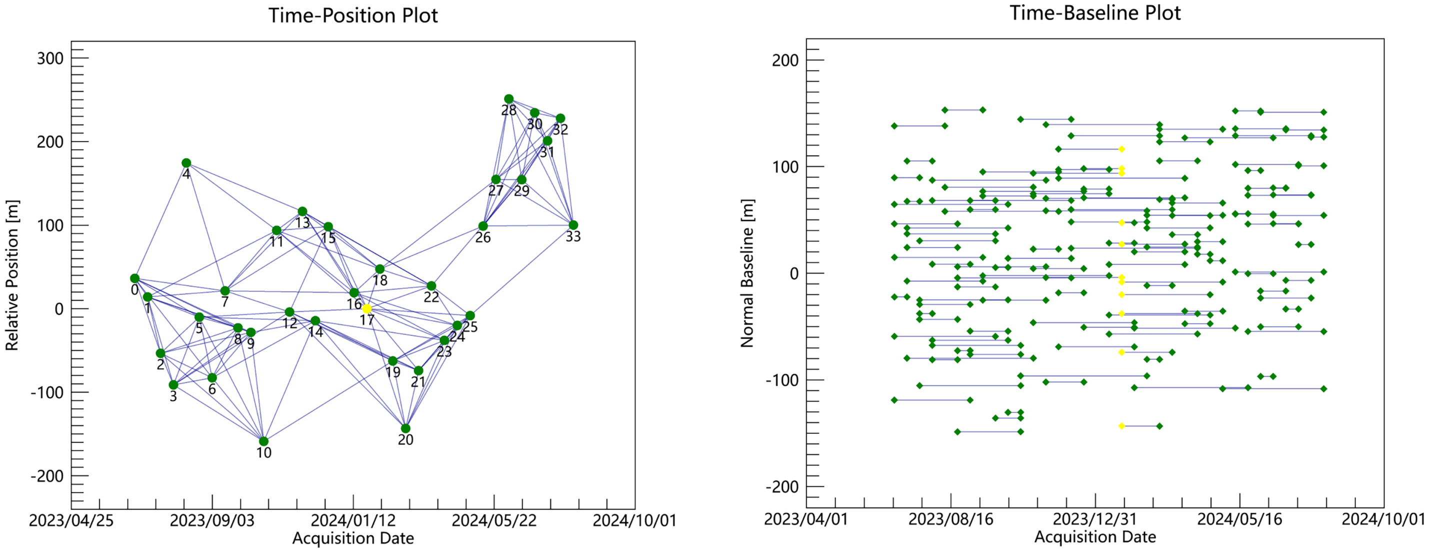

(A)

(B)

Figure 5 **(A) The spatial baseline of each interferometric pair; (B) the temporal baseline of each interferometric pair.**

Full-size DOI: 10.7717/peerj-cs.3327/fig-5

long-term information by integrating the previous cell state C_{t-1} and the candidate cell state $\tilde{C}_t$.

SBAS-INSAR MONITORING RESULTS AND ANALYSIS

Mine surface subsidence monitoring and identification

This study processed 34 Sentinel-1A images covering the study area (June 23, 2023–August 4, 2024) using SBAS-InSAR technology. To effectively reduce temporal and spatial decorrelation, the temporal baseline threshold was set to 120 days. The spatial baseline threshold was controlled within 3% of the critical baseline. This configuration generated 134 interferometric pairs (Fig. 5).

During data processing, a coherence threshold of 0.3 was applied. This threshold selected high-coherence points to ensure stability for subsequent analysis. A 30-m resolution DEM of the study area was introduced. This DEM removed topographic phase contributions. Goldstein filtering optimized the interferogram quality. Phase unwrapping was completed using the minimum cost flow (MCF) method.

Atmospheric delay and residual topographic errors were addressed through two SBAS-InSAR inversion iterations. The first inversion separated atmospheric phase from deformation signals. The second inversion further corrected residual errors. This iterative approach effectively enhanced deformation extraction accuracy.

Vertical deformation dominates surface movements in mining areas. This dominance justifies converting line-of-sight (LOS) displacements to vertical deformations. The processing yields annual average vertical deformation rate and cumulative settlement time series for Yinying Coal Mine.

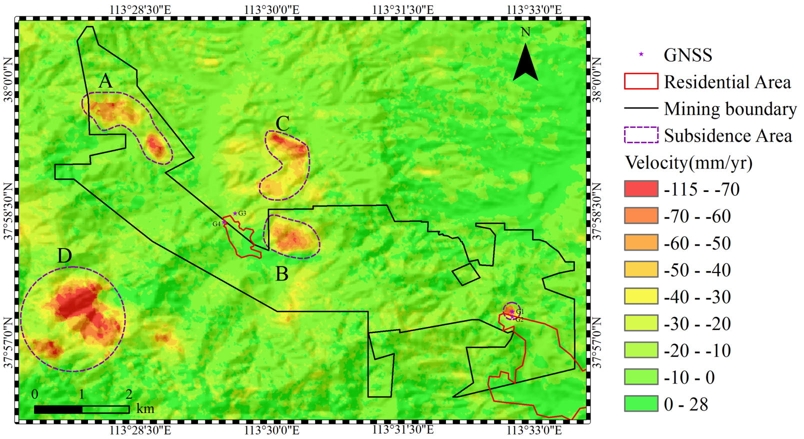

Figure 6 **Deformation rate map of the study area (negative values indicate subsidence; positive values indicate uplift).** Terrain shading base map from TianDiTu (www.tianditu.gov.cn).

Full-size DOI: 10.7717/peerj-cs.3327/fig-6

Figure 6 displays the annual deformation rate map of the study area from June 23, 2023 to August 4, 2024. The figure reveals annual deformation rate ranging from −115 to 28 mm/yr. The maximum subsidence rate reaches −115 mm/yr. Four distinct subsidence areas are identified in the study area. Subsidence areas A and B are located within the mining boundaries of Yinying Coal Mine. Subsidence areas C and D occur in adjacent mining areas. Area A covers 1.04 km^2, and Area B spans 0.64 km^2. Field investigations confirm both areas are active coal mining zones. The observed subsidence patterns align with on-site geological conditions.

Reliability analysis of monitoring results

To validate the reliability of ascending-orbit SBAS-InSAR monitoring results, this study employed dual validation methods: cross-validation using ascending/descending data and comparison with Global Navigation Satellite System (GNSS) measurements (*Tran et al., 2020*; *Chen et al., 2025*). First, 17 descending-orbit RADARSAT-2 images (June 21, 2023 to August 2, 2024) were processed using SBAS-InSAR with consistent parameters (120-day temporal baseline, 3% spatial baseline threshold, 0.3 coherence threshold), generating 36 interferometric pairs with the December 30, 2023 image as the master image. Processing steps followed the same workflow as "Mine Surface Subsidence Monitoring and Identification", including DEM-based flat-earth phase removal, Goldstein filtering, MCF unwrapping, and two inversion iterations for error correction.

Comparative analysis extracts 3,000 high-coherence points from subsidence areas. Figure 7 demonstrates agreement between ascending (Sentinel-1A) and descending (RADARSAT-2) orbit SBAS-InSAR results. The Pearson correlation coefficient reaches 0.946. This high consistency confirms the high consistency between both datasets.

Furthermore, we collected GNSS monitoring data from four stations. These stations were distributed across the subsidence area in the eastern part of the mining area and residential area west of Region B. We compared GNSS-derived cumulative subsidence time

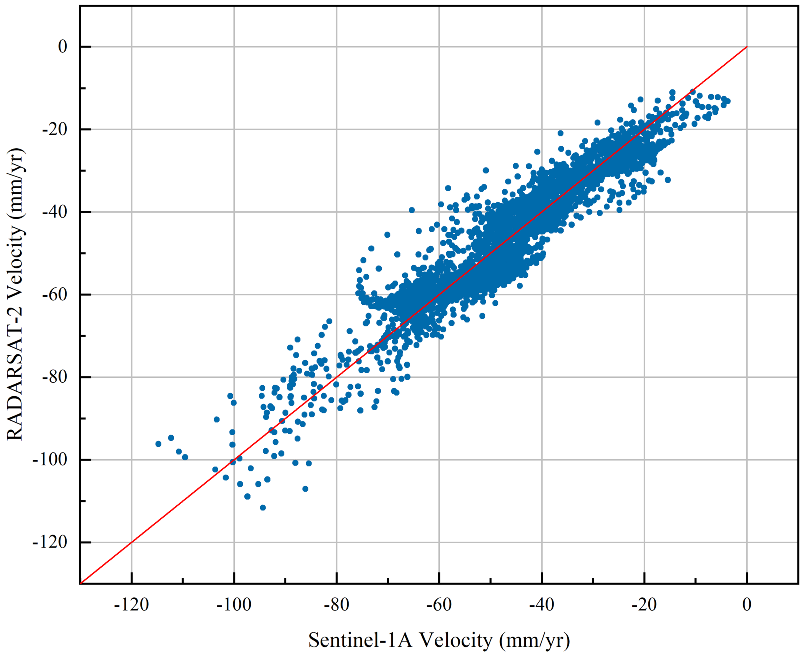

Figure 7 **Comparative analysis of deformation correlation at homologous points from multi-source monitoring data.** Full-size DOI: 10.7717/peerj-cs.3327/fig-7

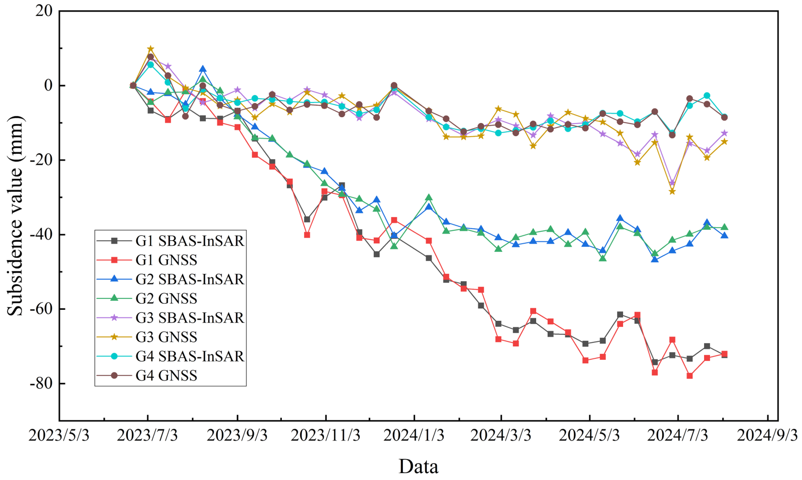

Figure 8 **Comparison of SBAS-InSAR and GNSS results.** Full-size DOI: 10.7717/peerj-cs.3327/fig-8

series against SBAS-InSAR results. Figure 8 shows the comparisons: The maximum absolute errors between both monitoring results were 4.684, 3.328, 3.194, and 2.462 mm for points G1, G2, G3, and G4, respectively. GNSS and InSAR deformation trends showed good agreement.

Both validation approaches confirm SBAS-InSAR result reliability. This technique is suitable for mining subsidence monitoring applications.

DISCUSSION

Characteristics of subsidence basin

To further analyze the deformation characteristics and patterns of the subsidence basin, this study selects Area B as the primary research region. Area B exhibits moderate cumulative subsidence and average subsidence rates. Although Area D shows larger surface subsidence values, mining activities in Area D ceased around March 2024. Within this study's monitoring period (June 23, 2023 to August 4, 2024), mining only occurred during the first 8 months in Area D. The subsequent 5 months represented a residual subsidence phase. Consequently, Area D provides an insufficiently long effective subsidence time series. Capturing the complete characteristics of surface subsidence during active mining is difficult with such short data.

In contrast, Area B is the core mining area of the Yinying Coal Mine from 2023 to 2025. Area B offers a sufficiently long time series within the monitoring period. Furthermore, the mining advance information for the 150,302 working face within Area B is complete. This complete data enables better comparison with SBAS-InSAR monitoring results. Such comparisons better reflect the relationship between subsidence and mining progress.

Moreover, the subsidence characteristics in Area B closely align with the overall subsidence pattern of the mining region. This alignment effectively represents typical subsidence behavior under standard mining conditions. Selecting Area B for prediction enables a more accurate linkage between mining activity and the subsidence process. It also provides a reliable scenario for validating the prediction model's practicality. Consequently, results obtained from Area B offer greater reference value for subsidence early warning. Figure 9 illustrates the time-series subsidence plot of this subsidence basin.

The plot demonstrates progressive expansion of subsidence from northeast to southwest. Subsidence area B exhibits continuous downward movement between June 23, 2023 and August 4, 2024. A profile line is established along the mining face orientation. Twenty-five sampling points are selected at 32-m intervals from southwest to northeast along this profile. The SBAS-InSAR monitoring results provide cumulative subsidence time series at these points. These time-series data generate the temporal cumulative subsidence curve along the profile line. Figure 10A displays the time-series cumulative subsidence curve of the profile line derived from this analysis. Furthermore, six characteristic points (P1–P6) were selected at uniform 75-m intervals along the profile line. These points comprehensively cover the subsidence basin's gradient zone from the center to the margin. P1 and P2 are located at the subsidence center. This area experiences the maximum mining impact, reflecting core extraction zone deformation. The surface cover consists of open woodland. This cover lacks dense root consolidation, making it highly susceptible to subsidence from coal seam extraction. P3, P4, and P5 lie within the subsidence transition zone. Moderate subsidence here illustrates the subsidence funnel expansion process. The surface cover is shrubland. Dense shrub roots provide topsoil consolidation, mitigating coal mining impacts. P6 is positioned at the subsidence margin. Minor subsidence here reflects indirect mining disturbance. The surface cover is farmland.

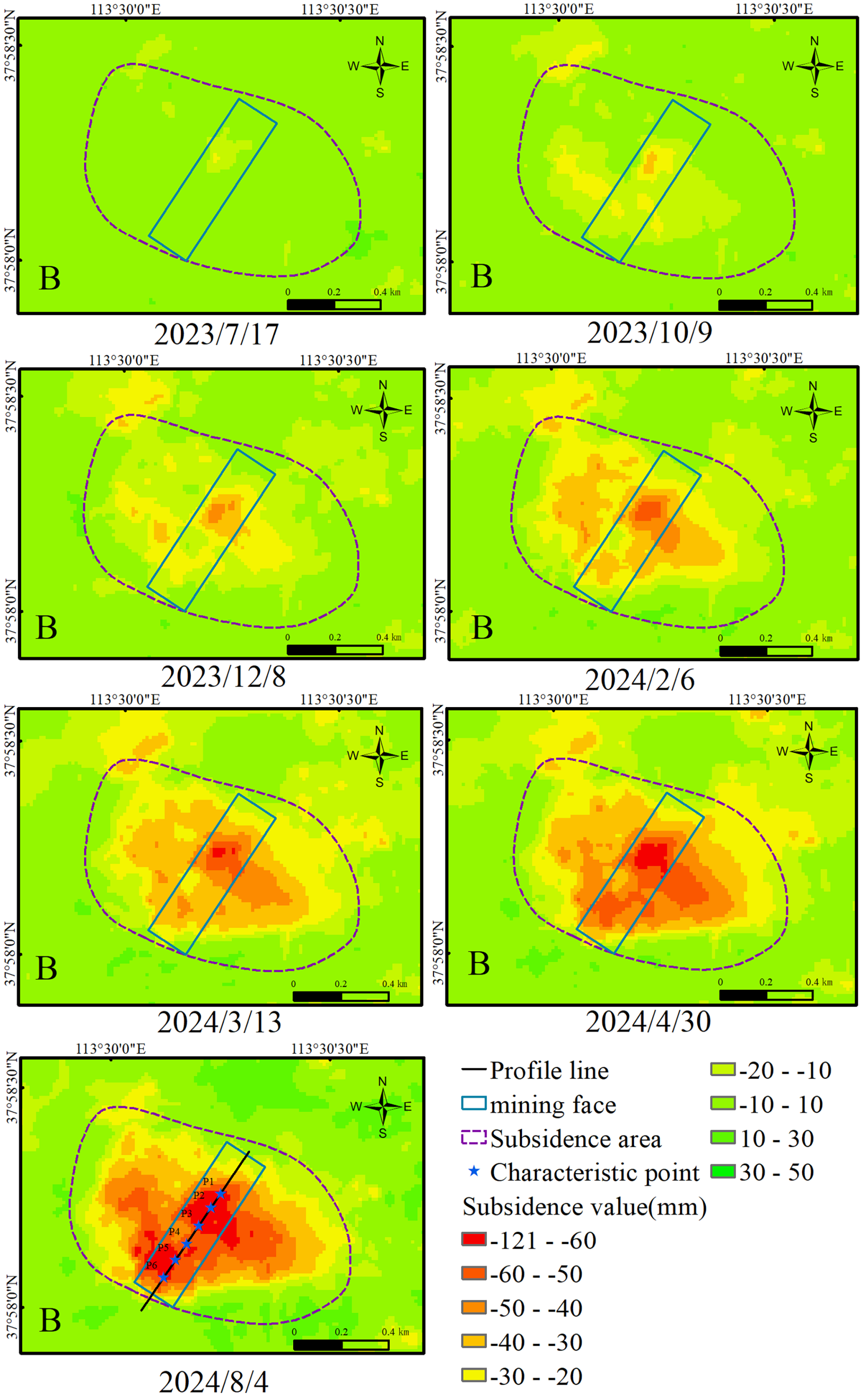

Figure 9 **Time-series subsidence plot of subsidence area B.**

Full-size DOI: 10.7717/peerj-cs.3327/fig-9

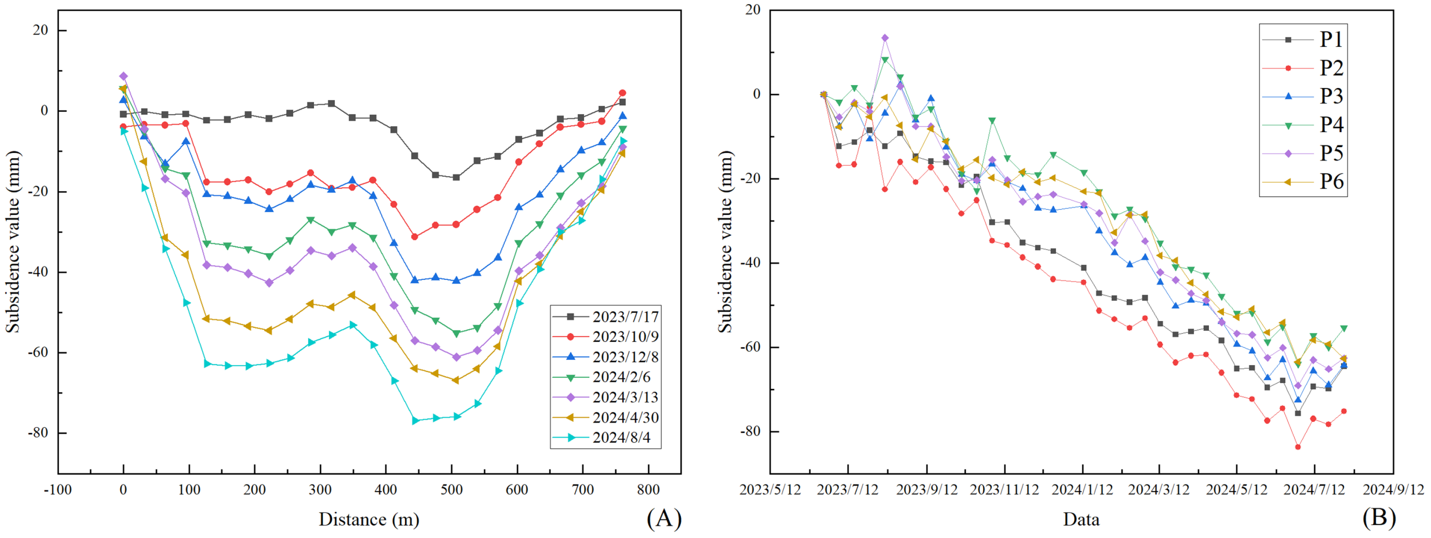

Figure 10 **(A) Time-series cumulative subsidence curve of the profile line; (B) Subsidence of the characteristic points with time.**
Full-size DOI: 10.7717/peerj-cs.3327/fig-10

Loose soil structure and severe erosion make this farmland vulnerable to mining-induced subsidence. These six points form a uniform distribution along the working face's strike-direction profile line. They collectively represent the subsidence center, transition zone, and margin area. This distribution effectively captures Area B's subsidence patterns.

Figures 9 and 10 reveal the evolution of surface subsidence in area B corresponding to the advance of the 150,302 mining face. The mining face advanced from northeast to southwest starting in June 2023. By July 17, 2023, SBAS-InSAR monitoring detected initial subsidence near the northeastern end of the face. This subsidence formed a small funnel-shaped area with a maximum cumulative subsidence of approximately −20 mm. The surface response was initial at this stage due to the short advance distance. Subsequently, the mining face continued advancing. By October 9, 2023, SBAS-InSAR monitoring showed the subsidence area expanding southwestward, covering the extracted portion of the face. The maximum cumulative subsidence increased to −36 mm, and the subsidence funnel elongated along the face strike. Simultaneously, slight subsidence appeared in surrounding areas affected by indirect mining disturbance.

By March 13, 2024, the mining face had advanced to its central section. SBAS-InSAR monitoring indicated continued subsidence across the affected area. The maximum cumulative subsidence reached −63 mm. However, the spatial extent of the subsidence area showed no significant increase compared to February 6, 2024. From March 13, 2024, to August 2024, the mining face advanced further towards the southwestern end. SBAS-InSAR monitoring then showed the subsidence area fully covering the mining face and a surrounding zone within 300 m. The subsidence center moved approximately 80 m southwestward. The average subsidence value of the subsidence center is −78 mm. Subsidence continued within the existing surrounding disturbance zone, but no significant new subsidence areas emerged.

Table 2 Parameter search spaces for Prophet and LSTM.

Prophet		**LSTM**	
Parameter name	Search space	Parameter name	Search space
seasonality_prior_scale	(0, 1)	hidden_size	(1, 64)
weekly_seasonality	(True, False)	time_window	(1, 25)
changepoint_prior_scale	(0, 1)	num_epochs	(1, 128)
changepoint_range	(0.4, 1)	num_layers	(1, 3)
seasonality_mode	(multiplicative, additive)		

Furthermore, Fig. 10A shows higher subsidence rates occurred in the northeastern part of the face between June 2023 and February 6, 2024. After the mining advance reached the central section on March 13, 2024, the subsidence rate decreased in the northeastern part but increased in the southwestern part. This differential subsidence rate further demonstrates the direct link between surface movement and mining face activity.

In summary, the direction of subsidence area expansion and the migration path of the subsidence center in Area B, monitored by SBAS-InSAR, synchronized precisely with the mining face advance. SBAS-InSAR also clearly captured the subsidence response in areas indirectly disturbed by mining. These observations confirm the spatial and temporal correlation between mining activity and surface deformation.

Bayesian optimization-based hyperparameter tuning

To optimize hyperparameters for Prophet and LSTM models, this study randomly selects 10 high-coherence subsidence points in the study area. SBAS-InSAR-derived time-series subsidence data are acquired for these points. The first 27 steps form the training set, while the last seven steps serve as the testing set. Mean absolute error (MAE) is selected as the evaluation metric for prediction performance.

The parameter search spaces for Prophet and LSTM are defined as specified in Table 2. The Bayesian optimization framework yields the following optimal configurations: Prophet (seasonality prior scale = 0.008, weekly seasonality = True, changepoint prior scale = 0.69, changepoint range = 0.5, seasonality mode = 'additive'); LSTM (hidden size = 17, time window = 18, num epochs = 61, num layers = 2).

Model prediction and results analysis

Characteristic point prediction and model performance comparison

This study extracted time-series cumulative subsidence data of six characteristic points in subsidence area B using SBAS-InSAR technology. The first 27 steps of data for each characteristic point served as the training set, and the subsequent seven steps as the validation set. The Prophet model and LSTM model with hyperparameter optimization were employed to predict subsidence for the subsequent 12 steps, The first seven steps of the prediction results were compared with the validation set, while the last five steps were used to demonstrate the future deformation trends. Two accuracy metrics were introduced

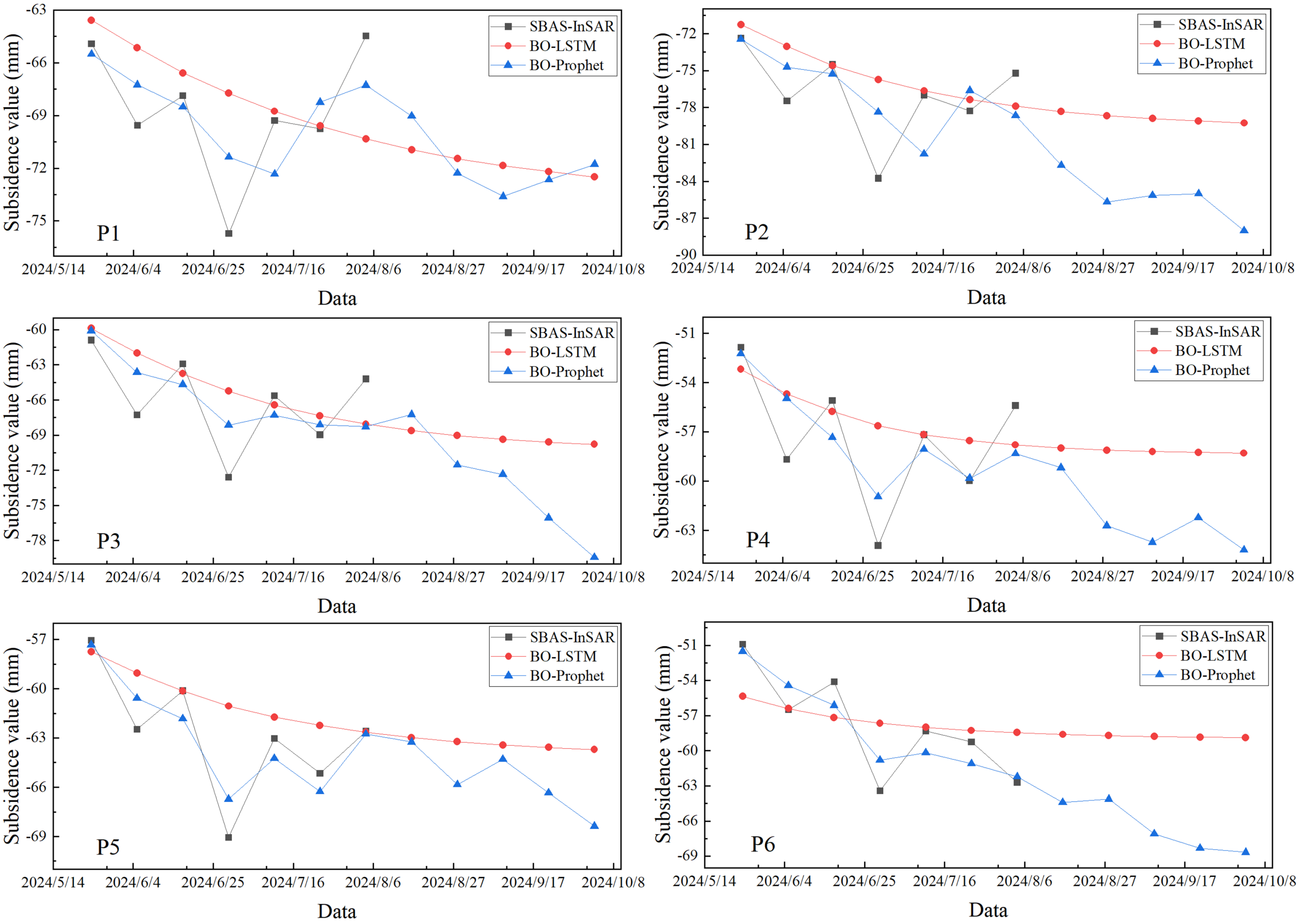

Figure 11 **Comparison of prediction results of each prediction model for each characteristic point.**

Full-size DOI: 10.7717/peerj-cs.3327/fig-11

to evaluate model performance: MAE and root mean square error (RMSE). The formulas are defined as follows:

$$MAE = \frac{1}{n}\sum_{i=1}^{n}\left|y_i - \hat{y}_i\right| \tag{10}$$

$$RMSE = \sqrt{\frac{1}{n}\sum_{i=1}^{n}\left(y_i - \hat{y}_i\right)^2}. \tag{11}$$

In these formulas, y_i represents measured values, $\hat{y}_i$ denotes predicted values. Using MAE and RMSE, this study systematically compared the Prophet and LSTM models. The analysis revealed performance differences in subsidence prediction, providing a scientific basis for model selection.

Figure 11 illustrates the comparative performance of the prediction models. The BO-Prophet model exhibits specific error distribution characteristics across seven

Table 3 Comparison table of the accuracy of each prediction model.

Point	BO-LSTM		BO-Prophet	
	MAE/mm	RMSE/mm	MAE/mm	RMSE/mm
P1	3.08	4.16	2.18	2.52
P2	2.52	3.65	2.69	3.26
P3	2.96	3.81	2.46	2.85
P4	2.59	3.44	1.90	2.31
P5	2.34	3.52	1.25	1.45
P6	2.69	3.41	1.63	1.79

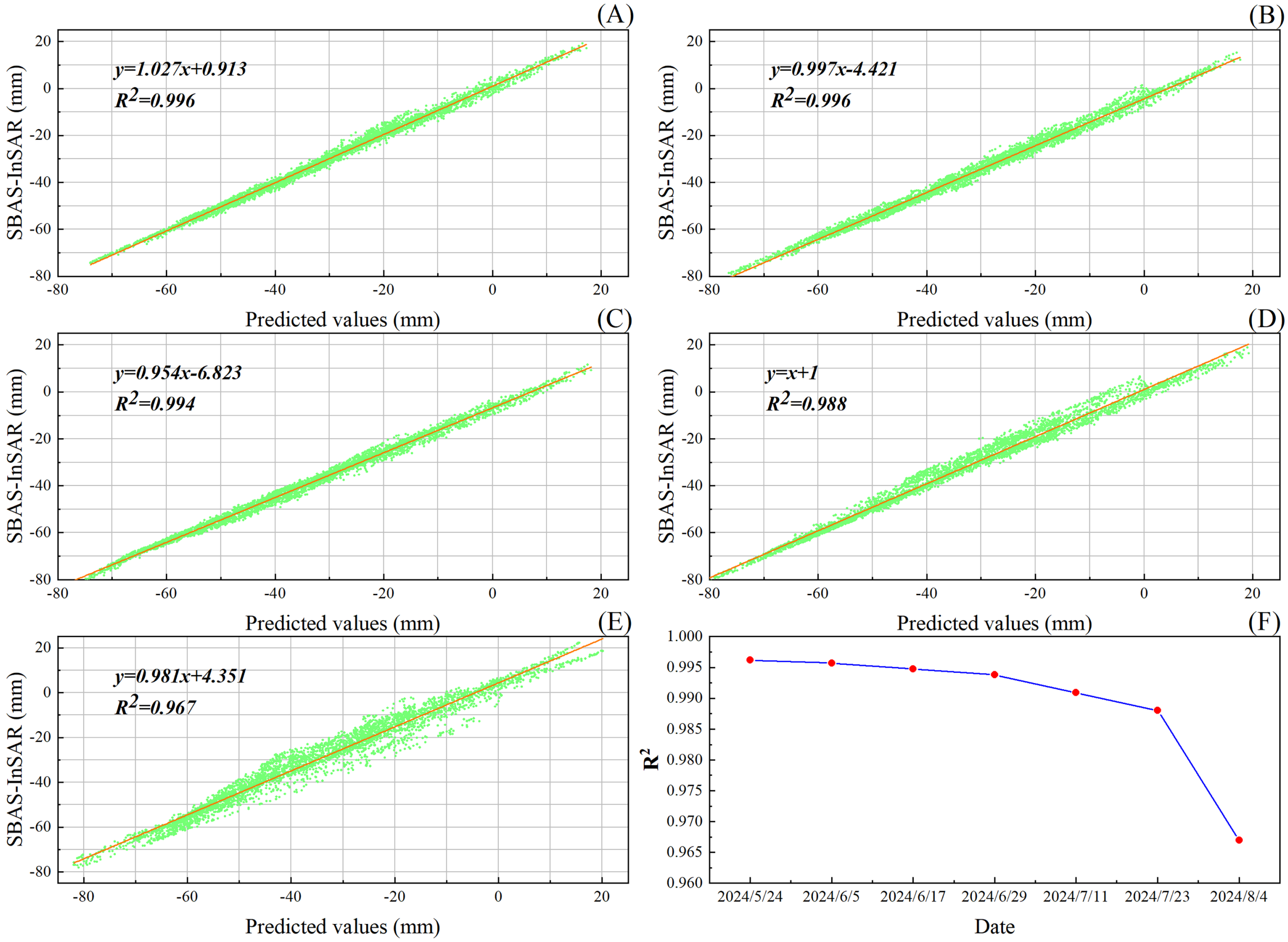

Figure 12 Correlation analysis between SBAS InSAR and prediction results: (A) 12d; (B) 24d; (C) 48d; (D) 72d; (E) 84d; (F) R^2 changes over different time spans.

Full-size DOI: 10.7717/peerj-cs.3327/fig-12

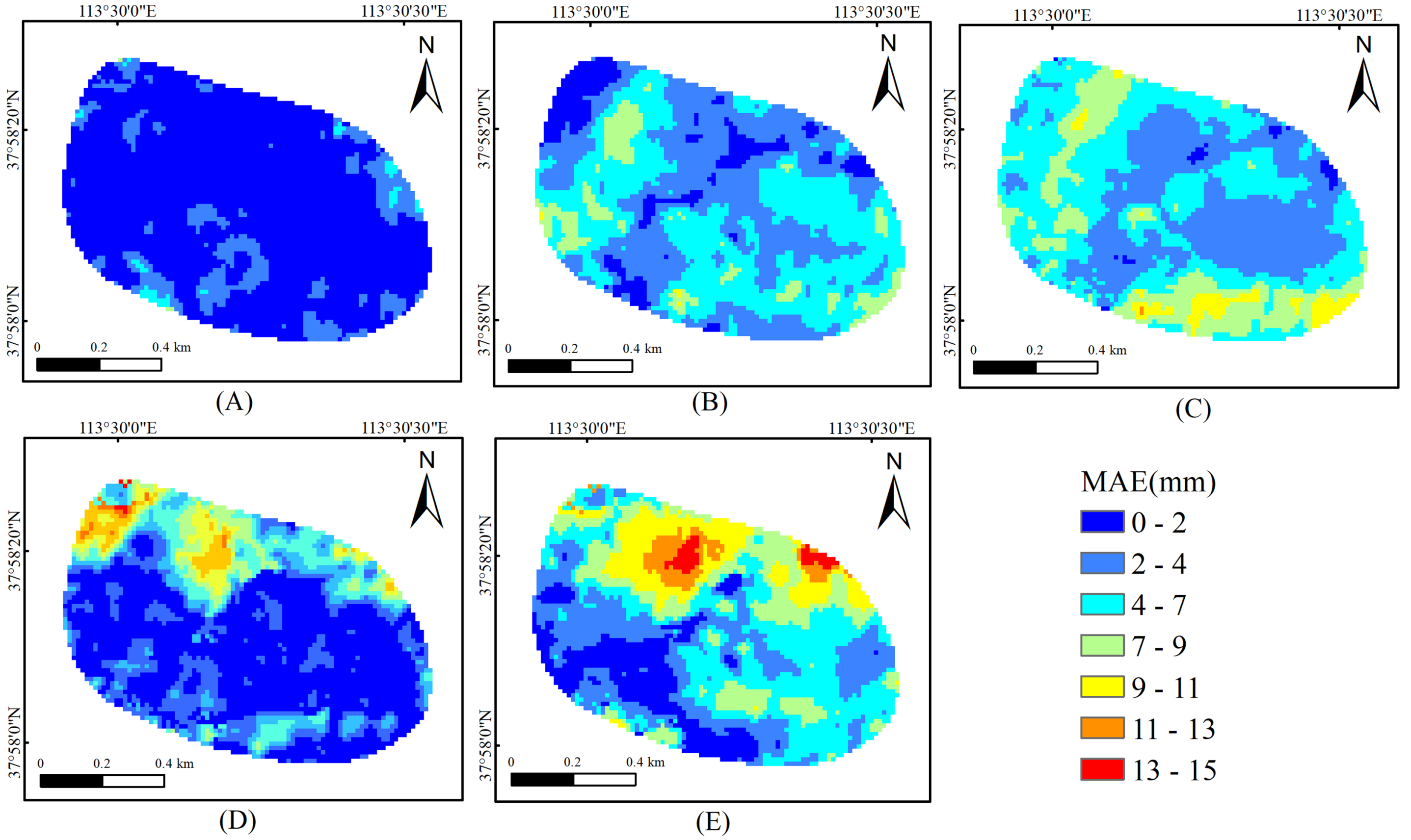

Figure 13 **The spatial distribution map of prediction errors in area B. (A) 12d; (B) 24d; (C) 48d; (D) 72d; (E) 84d.**

Full-size DOI: 10.7717/peerj-cs.3327/fig-13

prediction periods for six characteristic points. The maximum absolute error values for each characteristic point are 4.35, 5.38, 4.45, 3.72, 2.33, and 2.63 mm. Notably, the maximum absolute error for all characteristic points (except P4) concentrates in the third prediction step. This trend aligns with significant subsidence observed in Area B from June 17 to June 29, 2024.

The minimum absolute errors of the BO-Prophet model at six points are 0.59, 0.09, 0.79, 0.15, 0.27, and 0.48 mm. These values confirm high consistency between the BO-Prophet predictions and SBAS-InSAR monitoring data. Visual comparisons demonstrate strong agreement between predicted results and monitoring data.

According to the error indicators presented in Table 3, the BO-Prophet model achieves MAE values of 2.18, 2.69, 2.46, 1.90, 1.25, and 1.63 mm across the six characteristic points. The RMSE values are 2.52, 3.26, 2.85, 2.31, 1.45, and 1.79 mm. Compared to the BO-LSTM model, the BO-Prophet model shows lower errors in both MAE and RMSE. These results validate the higher accuracy and stability of the BO-Prophet model in predicting surface subsidence.

To comprehensively assess prediction accuracy, the BO-Prophet model generated subsidence forecasts across area B. These predictions were compared with SBAS-InSAR measurements through correlation analysis. Figure 12 demonstrates strong consistency between predicted values and SBAS-InSAR values across multiple time spans (12d, 24d, 48d, 72d, 84d). All correlation coefficients exceed 0.96, confirming the model's effectiveness in large-scale subsidence prediction. Further analysis examines correlation coefficient variations under different time spans. As shown in Fig. 12F, the coefficients gradually decrease over time. This trend indicates diminishing prediction accuracy with increasing forecast duration.

Distribution of errors

The study investigates spatial error patterns by overlaying BO-Prophet predictions with SBAS-InSAR measurements in area B. This process absolute error distribution map. Figure 13 reveals two critical trends. First, prediction errors progressively increase over time. Second, errors predominantly cluster in the northwestern sector of area B. This area corresponds to the marginal slow subsidence zone of the depression basin. These findings demonstrate BO-Prophet's superior short-term forecasting capability. However, error accumulation becomes evident with extended prediction horizons. The spatial error concentration suggests systematic biases in specific geological subregions.

CONCLUSIONS

This study focused on the Yinying Coal Mine, utilizing SBAS-InSAR technology to obtain the annual average subsidence rate results and the time-series cumulative subsidence results of Yinying Coal Mine. Then, the study applied the BO-LSTM and BO-Prophet prediction models to forecast subsidence in the mining area, with each model implemented independently for comparative analysis. Key findings are summarized below:

(1) SBAS-InSAR monitoring results: The SBAS-InSAR monitoring results revealed an annual average subsidence rate of up to 115 mm/yr and a maximum cumulative subsidence of 121 mm between June 23, 2023, and August 2, 2024. Both values fell within normal ranges for mining-induced subsidence.

(2) Validation using multi-track data and GNSS: The reliability of SBAS-InSAR results was validated through independent processing of multi-track datasets (ascending and descending tracks) and comparison with GNSS measurements. A Pearson correlation coefficient of 0.946 confirmed high consistency between ascending and descending datasets. Comparisons with four GNSS stations showed maximum absolute errors of 4.684, 3.328, 3.194, and 2.462 mm, with good agreement in deformation trends.

(3) Spatial analysis of subsidence area B: Longitudinal profile analysis of Subsidence area B showed continuous growth in subsidence over time. The deformation exhibited a distinct funnel-shaped pattern, aligning with typical mining-induced subsidence characteristics.

(4) A comparative analysis evaluates two prediction models using standard performance metrics. The BO-Prophet (MAE = 2.02 mm, RMSE = 2.36 mm) demonstrates superior prediction accuracy over the BO-LSTM (MAE = 2.70 mm, RMSE = 3.67 mm). Further examination confirms high consistency ($R^2 > 0.96$) between BO-Prophet predictions and SBAS-InSAR monitoring results; BO-Prophet has a better prediction effect in

short-term predictions. This integration enables effective monitoring and forecasting of mining-induced subsidence. Implementing BO-Prophet with SBAS-InSAR technology enhances early warning systems for mining hazards. It supports disaster prevention and mitigation strategies in mining areas.

Future studies will focus on enhancing the model's robustness, generalizability, and rigor through integrated efforts. We will expand cross-site validation in diverse mining areas—including other Loess Plateau regions, high-steep mountain zones, and major coal-producing regions in Shanxi, Shaanxi, and Inner Mongolia—to verify its applicability beyond Yinying. We will also compare Bayesian optimization with alternatives (*e.g.*, genetic algorithms) to identify the most robust hyperparameter tuning strategy for varied scenarios. Additionally, we will strengthen multi-source validation by optimizing GNSS deployment and integrating supplementary ground data (leveling, uncrewed aerial vehicle (UAV) photogrammetry) to boost reliability of both monitoring and prediction. Finally, we will advance the framework with physics-constrained deep learning and spatiotemporal attention mechanisms to address long-term error accumulation and sensitivity to geological heterogeneities. These efforts will refine early warning capabilities, support data-driven disaster prevention, and promote sustainable mining practices.

ACKNOWLEDGEMENTS

The author thanks the European Space Agency (ESA) for providing free Sentinel-1A SAR images and NASA (National Aeronautics and Space Administration) for providing free SRTM DEM data. The author also thanks AI (DeepSeek) for its assistance in English translation work. Additionally, the author is grateful to the anonymous reviewers and the journal editors for their valuable suggestions and guidance.

ADDITIONAL INFORMATION AND DECLARATIONS

Funding

This work was supported by the Shanxi Provincial Natural Science Foundation (No. 202103021223381). The funders had no role in study design, data collection and analysis, decision to publish, or preparation of the manuscript.

Grant Disclosures

The following grant information was disclosed by the authors:
Shanxi Provincial Natural Science Foundation: 202103021223381.

Competing Interests

The authors declare that they have no competing interests.

Author Contributions

- Kangjie Yu conceived and designed the experiments, performed the experiments, analyzed the data, performed the computation work, prepared figures and/or tables, authored or reviewed drafts of the article, and approved the final draft.

Data Availability

The following information was supplied regarding data availability:

The raw measurements are available in the Supplemental Files.

Supplemental Information

Supplemental information for this article can be found online at http://dx.doi.org/10.7717/peerj-cs.3327#supplemental-information.

REFERENCES

Aobpaet A, Cuenca MC, Hooper A, Trisirisatayawong I. 2013. InSAR time-series analysis of land subsidence in Bangkok, Thailand. *International Journal of Remote Sensing* **34(8)**:2969–2982 DOI 10.1080/01431161.2012.756596.

Bai X, Ding H, Lian J, Ma D, Yang X, Sun N, Xue W, Chang Y. 2020. Coal production in China: past, present, and future projections. In: Dai S, Finkelman RB, eds. *Coal Geology of China*. First Edition. Oxfordshire, UK: Routledge, 1–13.

Berardino P, Fornaro G, Lanari R, Sansosti E. 2002. A new algorithm for surface deformation monitoring based on small baseline differential SAR interferograms. *IEEE Transactions on Geoscience and Remote Sensing* **40(11)**:2375–2383 DOI 10.1109/tgrs.2002.803792.

Bi Z, Li S, Zhang L, Zhang W, Li Y, Yuan L. 2024. Multi-track sequential InSAR mining 3D deformation monitoring and prediction combined with Prophet-CNN model. *Bulletin of Surveying and Mapping* **2024(5)**:53–59 DOI 10.13474/j.cnki.11-2246.2024.0510.

Bischl B, Binder M, Lang M, Pielok T, Richter J, Coors S, Thomas J, Ullmann T, Becker M, Boulesteix AL, Deng D, Lindauer M. 2023. Hyperparameter optimization: foundations, algorithms, best practices, and open challenges. *Wiley Interdisciplinary Reviews: Data Mining and Knowledge Discovery* **13(2)**:e1484 DOI 10.1002/widm.1484.

Cai Y, Jin Y, Wang Z, Chen T, Wang Y, Kong W, Xiao W, Li X, Lian X, Hu H. 2023. A review of monitoring, calculation, and simulation methods for ground subsidence induced by coal mining. *International Journal of Coal Science & Technology* **10**:32 DOI 10.1007/s40789-023-00595-4.

Chang H, Yang Z, Zhang Y. 2025. Forecasting daily freight flow in cold regions of China using the hybrid Prophet model considering the importance of festivals and epidemic prevention policy. *Research in Transportation Business & Management* **59(12)**:101294 DOI 10.1016/j.rtbm.2025.101294.

Chen L, Fan Y, Xiao H, Wan J, Chen L. 2025. Prediction and analysis of mining area surface subsidence based on time series InSAR and IRIME-LSTM model. *Remote Sensing for Natural Resources* **37**:245–252 DOI 10.6046/zrzyyg.2024048.

Chérif H, Snoun H, Bellakhal G, Kanfoudi H. 2023. Forecasting of ozone concentrations using the Neural Prophet model: application to the Tunisian case. *Euro-Mediterranean Journal for Environmental Integration* **8(4)**:987–998 DOI 10.1007/s41207-023-00414-x.

Chu C, Muradian N. 2016. Safety and environmental implications of coal mining. *International Journal of Environment and Pollution* **59**:250–268 DOI 10.1504/IJEP.2016.079899.

Deng Z, Xu L, Li Y, Chen Y, Su N, He Y. 2025. Subgrade cumulative deformation probabilistic prediction method based on machine learning. *Soil Dynamics and Earthquake Engineering* **191(1)**:109233 DOI 10.1016/j.soildyn.2025.109233.

Dongwei Q, Yuci T, Yuzheng W, Keliang D, Tiancheng L, Shanshan W. 2024. Land subsidence analysis along high-speed railway based on EEMD-Prophet method. *Scientific Reports* **14(1)**:732 DOI 10.1038/s41598-024-51174-9.

Dontala SP, Reddy TB, Vadde R. 2015. Environmental aspects and impacts its mitigation measures of corporate coal mining. *Procedia Earth and Planetary Science* **11**:2–7 DOI 10.1016/j.proeps.2015.06.002.

Du Q, Li G, Zhou Y, Chai M, Chen D, Qi S, Wu G. 2021. Deformation monitoring in an Alpine mining area in the Tianshan Mountains based on SBAS-InSAR technology. *Advances in Materials Science and Engineering* **2021(1)**:9988017 DOI 10.1155/2021/9988017.

Fan H, Deng K, Ju C, Zhu C, Xue J. 2011. Land subsidence monitoring by D-InSAR technique. *Mining Science and Technology (China)* **21(6)**:869–872 DOI 10.1016/j.mstc.2011.05.030.

Guo H, Yuan Y, Wang J, Cui J, Zhang D, Zhang R, Cao Q, Li J, Dai W, Bao H. 2023. Large-scale land subsidence monitoring and prediction based on SBAS-InSAR technology with time-series sentinel-1A satellite data. *Remote Sensing* **15(11)**:2843 DOI 10.3390/rs15112843.

Habib MA, Khan R. 2021. Environmental impacts of coal-mining and coal-fired power-plant activities in a developing country with global context. *Environmental Challenges and Solutions* **25(1)**:421–493 DOI 10.1007/978-3-030-63422-3_24.

He L, Wu D, Ma L. 2023. Numerical simulation and verification of goaf morphology evolution and surface subsidence in a mine. *Engineering Failure Analysis* **144(3)**:106918 DOI 10.1016/j.engfailanal.2022.106918.

Hejmanowski R, Malinowska A. 2009. Evaluation of reliability of subsidence prediction based on spatial statistical analysis. *International Journal of Rock Mechanics and Mining Sciences* **46(2)**:432–438 DOI 10.1016/j.ijrmms.2008.07.012.

Khan BA, Zhao C, Kakar N, Chen X. 2025. SBAS-InSAR monitoring of landslides and glaciers along the Karakoram highway between China and Pakistan. *Remote Sensing* **17(4)**:605 DOI 10.3390/rs17040605.

Li S, Xu W, Li Z. 2022. Review of the SBAS InSAR time-series algorithms, applications, and challenges. *Geodesy and Geodynamics* **13(2)**:114–126 DOI 10.1016/j.geog.2021.09.007.

Li H, Zha J, Guo G. 2019. A new dynamic prediction method for surface subsidence based on numerical model parameter sensitivity. *Journal of Cleaner Production* **233(2)**:1418–1424 DOI 10.1016/j.jclepro.2019.06.208.

Li T, Zhang H, Fan H, Zheng C, Liu J. 2021. Position inversion of goafs in deep coal seams based on DS-InSAR data and the probability integral methods. *Remote Sensing* **13(15)**:2898 DOI 10.3390/rs13152898.

Liu J, Ma F, Li G, Guo J, Wan Y, Song Y. 2022. Evolution assessment of mining subsidence characteristics using SBAS and PS interferometry in Sanshandao Gold Mine, China. *Remote Sensing* **14(2)**:290 DOI 10.3390/rs14020290.

Ma F, Sui L, Lian W. 2023. Prediction of mine subsidence based on InSAR technology and the LSTM algorithm: a case study of the Shigouyi Coalfield, Ningxia (China). *Remote Sensing* **15(11)**:2755 DOI 10.3390/rs15112755.

Santos SMd, Cabral JJd SP, Pontes Filho IDd S. 2012. Monitoring of soil subsidence in urban and coastal areas due to groundwater overexploitation using GPS. *Natural Hazards* **64(1)**:421–439 DOI 10.1007/s11069-012-0247-9.

Sevil J, Benito-Calvo A, Gutiérrez F. 2021. Sinkhole subsidence monitoring combining terrestrial laser scanner and high-precision levelling. *Earth Surface Processes and Landforms* **46(8)**:1431–1444 DOI 10.1002/esp.5112.

Shahriari B, Swersky K, Wang Z, Adams RP, De Freitas N. 2015. Taking the human out of the loop: a review of Bayesian optimization. *Proceedings of the IEEE* **104(1)**:148–175 DOI 10.1109/jproc.2015.2494218.

Shen Z, Santosh M, Arabameri A. 2023. Application of novel hybrid model for land subsidence susceptibility mapping. *Geological Journal* **58(6)**:2302–2320 DOI 10.1002/gj.4603.

Shi L, Gong H, Chen B, Zhou C. 2020. Land subsidence prediction induced by multiple factors using machine learning method. *Remote Sensing* **12(24)**:4044 DOI 10.3390/rs12244044.

Shi X, Zhong J, Yin Y, Chen Y, Zhou H, Wang M, Dai K. 2023. Integrating SBAS-InSAR and LSTM for subsidence monitoring and prediction at Hong Kong international airport. *Ore and Energy Resource Geology* **15(3)**:100032 DOI 10.1016/j.oreoa.2023.100032.

Smagulova K, James AP. 2019. A survey on LSTM memristive neural network architectures and applications. *The European Physical Journal Special Topics* **228(10)**:2313–2324 DOI 10.1140/epjst/e2019-900046-x.

Snoek J, Larochelle H, Adams RP. 2012. Practical Bayesian optimization of machine learning algorithms. *Proceedings of the 26th International Conference on Neural Information Processing Systems* **2**:25.

Taylor SJ, Letham B. 2018. Forecasting at scale. *The American Statistician* **72(1)**:37–45 DOI 10.1080/00031305.2017.1380080.

Tran VA, Bui X-N, Nguyen QL, Tran TA. 2020. Land subsidence detection in Tan My-Thuong Tan Open Pit Mine and surrounding areas by time series of Sentinel-1 images. *Journal of the Polish Mineral Engineering Society* **1(2)**:171–180 DOI 10.29227/im-2020-02-22.

Wang X, Diao M, Guo H, Wang L, Guo H, Li D. 2024. Landslide deformation prediction and automatic warning by coupling machine learning and physical models. *Earth and Space Science* **11(6)**:343 DOI 10.1029/2023ea003238.

Wang J, Wu S, Wang Z, Barbaryka A, Tost M, Li M. 2025. New prediction method of subsidence based on the numerical displacement analysis: a study case of deep-buried thick alluvial layer and thin bedrock. *Rock Mechanics and Rock Engineering* **58**:6723–6744 DOI 10.1007/S00603-025-04459-Y.

Wu PC, Wei M, D'Hondt S. 2022. Subsidence in coastal cities throughout the world observed by InSAR. *Geophysical Research Letters* **49(7)**:e2022GL098477 DOI 10.1029/2022gl098477.

Yang J, Kou P, Dong X, Xia Y, Gu Q, Tao Y, Feng J, Ji Q, Wang W, Avtar R. 2025. Reservoir water level decline accelerates ground subsidence: InSAR monitoring and machine learning prediction of surface deformation in the Three Gorges Reservoir area. *Frontiers in Earth Science* **12**:1503634 DOI 10.3389/feart.2024.1503634.

Yu Y, Si X, Hu C, Zhang J. 2019. A review of recurrent neural networks: LSTM cells and network architectures. *Neural Computation* **31(7)**:1235–1270 DOI 10.1162/neco_a_01199.

Zhang T, Shi Y, Wang J, Liu L, Yan Q. 2021. Analysis of subsidence prediction model based on InSAR and improved support vector machine. *Science of Surveying and Mapping* **46**:63–70 DOI 10.16251/j.cnki.1009-2307.2021.11.010.

Zhu M, Yu X, Tan H, Yuan J. 2024. Integrated high-precision monitoring method for surface subsidence in mining areas using D-InSAR, SBAS, and UAV technologies. *Scientific Reports* **14(1)**:12445 DOI 10.1038/s41598-024-63400-5.